

Northumbria Research Link

Citation: Wang, Xi, Liu, Changxu, Gao, Congcong, Yao, Kaili, Masouleh, Seyed Shayan Mousavi, Berté, Rodrigo, Ren, Haoran, Menezes, Leonardo de S., Cortés, Emiliano, Bicket, Isobel C., Wang, Haiyu, Li, Ning, Zhang, Zhenglong, Li, Ming, Xie, Wei, Yu, Yifu, Fang, Yurui, Zhang, Shunping, Xu, Hongxing, Vomiero, Alberto, Liu, Yongchang, Botton, Gianluigi A., Maier, Stefan A. and Liang, Hongyan (2021) Self-Constructed Multiple Plasmonic Hotspots on an Individual Fractal to Amplify Broadband Hot Electron Generation. ACS Nano, 15 (6). pp. 10553-10564. ISSN 1936-0851

Published by: American Chemical Society

URL: <https://doi.org/10.1021/acsnano.1c03218>
<<https://doi.org/10.1021/acsnano.1c03218>>

This version was downloaded from Northumbria Research Link:
<http://nrl.northumbria.ac.uk/id/eprint/47179/>

Northumbria University has developed Northumbria Research Link (NRL) to enable users to access the University's research output. Copyright © and moral rights for items on NRL are retained by the individual author(s) and/or other copyright owners. Single copies of full items can be reproduced, displayed or performed, and given to third parties in any format or medium for personal research or study, educational, or not-for-profit purposes without prior permission or charge, provided the authors, title and full bibliographic details are given, as well as a hyperlink and/or URL to the original metadata page. The content must not be changed in any way. Full items must not be sold commercially in any format or medium without formal permission of the copyright holder. The full policy is available online: <http://nrl.northumbria.ac.uk/policies.html>

This document may differ from the final, published version of the research and has been made available online in accordance with publisher policies. To read and/or cite from the published version of the research, please visit the publisher's website (a subscription may be required.)

Self-constructed Multiple Plasmonic Hotspots on an Individual Fractal to Amplify Broadband Hot Electron Generation

*Xi Wang,^{a, b, #} Changxu Liu,^{c, #} Congcong Gao,^a Kaili Yao,^a Seyed Shayan Mousavi Masouleh,^d Rodrigo Berté,^c Haoran Ren,^c Leonardo de S. Menezes,^{c, e} Emiliano Cortés,^c Isobel Bicket,^d Haiyu Wang,^a Ning Li,^a Zenglong Zhang,^f Ming Li,^g Wei Xie,^h Yifu Yu,ⁱ Yurui Fang,^j Shunping Zhang,^k Hongxing Xu,^l Alberto Vomiero,^{m, n} Yongchang Liu,^{a, o, *} Gianluigi A. Botton,^{d, *} Stefan A. Maier,^{c, p, *} Hongyan Liang^{a, b, *}*

^a School of Materials Science and Engineering, Tianjin University, Tianjin 300350, P. R. China

^b Key Laboratory of Efficient Utilization of Low and Medium Grade Energy, Ministry of Education, Tianjin University, Tianjin 300350, P. R. China.

^c Chair in Hybrid Nanosystems, Nanoinstitut Munich, Faculty of Physics, Ludwig-Maximilians-Universität München, D-80539 München, Germany

^d Department of Materials Science and Engineering, McMaster University, 1280 Main Street W., Hamilton, Ontario L8S 4L7, Canada

^e Departamento de Física, Universidade Federal de Pernambuco, BR-50670901 Recife-PE, Brazil

^f School of Physics and Information Technology, Shaanxi Normal University, Xi'an 710061, P. R. China

^g School of Materials Science and Engineering, State Key Laboratory for Power Metallurgy, Central South University, Changsha, Hunan 410083, P. R. China

^h Key Lab of Advanced Energy Materials Chemistry (Ministry of Education), Renewable Energy Conversion and Storage Center, College of Chemistry, Nankai University, Weijin Road 94, Tianjin 300071, P. R. China

ⁱ Department of Chemistry, School of Science, Institute of Molecular Plus, Tianjin University, Tianjin, 300072, China

^j Key Laboratory of Materials Modification by Laser, Electron, and Ion Beams (Ministry of Education), School of Physics, Dalian University of Technology, Dalian 116024, P. R. China

^k School of Physics and Technology, Center for Nanoscience and Nanotechnology, and Key Laboratory of Artificial Micro- and Nano-structures of Ministry of Education, Wuhan University, Wuhan 430072, P. R. China

^l The Institute for Advanced Studies and School of Physics and Technology, Center for Nanoscience and Nanotechnology, and Key Laboratory of Artificial Micro- and Nano-structures of Ministry of Education, Wuhan University, Wuhan 430072, P. R. China

^m Division of Materials Science, Department of Engineering Sciences and Mathematics, Luleå University of Technology, S-97187 Luleå, Sweden

ⁿ Department of Molecular Sciences and Nanosystems, Ca' Foscari University of Venice, I-30172 Venezia Mestre, Italy

^o Tianjin Key Lab Advanced Joining Technology, Tianjin 300354, P. R. China

^p Department of Physics, Imperial College London, London SW7 2AZ, England

Corresponding Author

* E-mail: ycliu@tju.edu.cn

* E-mail: gbotton@mcmaster.ca

* E-mail: Stefan.Maier@physik.uni-muenchen.de

* E-mail: hongyan.liang@tju.edu.cn

ABSTRACT:

Plasmonic nanoparticles are ideal candidates for hot-electron-assisted applications, but their narrow resonance region and limited hot spot number hindered the energy utilization of broadband solar energy. Inspired by tree branches, we designed and chemically synthesized silver fractals, which enable self-constructed hot spots and multiple plasmonic resonances, extending the broadband generation of hot electrons for better matching with the solar radiation spectrum. We directly revealed the plasmonic origin, the spatial distribution, and the decay dynamics of hot electrons on the single-particle level by using *ab-initio* simulation, dark-field spectra, pump-probe measurements, and electron energy loss spectroscopy. Our results show that fractals with acute tips and narrow gaps can support broadband resonances (400 nm-1100 nm) and a large number of randomly distributed hot spots, which can provide unpolarized enhanced near field and promote hot electrons generation. As a proof-of-concept, hot-electron-triggered dimerization of para-nitrothiophenol and hydrogen production are investigated under various irradiation and the promoted hot electron generation on fractals was confirmed with significantly improved efficiency.

KEYWORDS: dendritic fractal, broadband hot electron generation, plasmonic resonances, electron energy loss spectroscopy (EELS), plasmon-assisted photocatalysis

Hot carriers generated *via* plasmon decay which can circumvent bandgap limitations suggest extensive applications, including photochemistry, photovoltaics, and photodetectors.¹⁻⁴ Hot carrier-driven photocatalysis with metallic nanoparticles (NPs) has greatly stimulated a better paradigm in harvesting photons, due to their ability to drive reactions under substantially milder conditions than traditional thermocatalysis.⁵ Plasmonically active metals such as Au,⁶⁻⁹ Ag,¹⁰⁻¹² Al,¹³ Cu¹⁴⁻¹⁶ and alloys¹⁷ have been applied for a set of chemical reactions, ranging from H₂-D₂ exchange,¹³ hydrogen evolution^{7, 8, 18} to CO₂ reduction,^{6, 19-22} selective oxidation reactions¹⁴ and ammonia decomposition.¹⁷ Meanwhile, transition metal nitrides including TiN with intrinsic broadband absorption were utilized for hot carrier assisted photocatalysis.^{23, 24}

The design and fabrication of plasmonic structures, which amplify the interaction of light, is crucial for the utilization of energy and charge carriers. However, the generation rate of hot electrons through surface scattering decreases with increasing excitation wavelength, as predicted by theoretical calculations^{25, 26} and observed in experiments.^{7, 8, 15, 17, 18} Considering the broadband feature of the solar spectrum with a large portion (~55%) of energy produced beyond 700 nm,²⁷ achieving hot-electron generation in the whole spectrum, is of substantial importance for improving the efficiency of photocatalysis and to meet the requirements from practical applications. To achieve this goal, broadband absorption covering the visible to the near-infrared (NIR) is a prerequisite. Despite the success of the synthesis of NPs with broadband absorption, hot electron generation is hindered by the limited number of hotspots, in which hot electron generation is amplified by localized electromagnetic (EM) field.^{28, 29} Hotspots are generally realized with interparticle interactions, the number of which is limited due to the difficulty and low reproducibility for the formation of sub-10 nm gaps.³⁰ More importantly, the anisotropic geometry makes the excitation of the hotspots strongly dependent on the incident light's polarization, and

hence unpolarized sunlight becomes inefficient in exciting these structures. Considering the substantial role of hotspots in hot carrier generation (providing the field enhancement and breaking of linear momentum due to a strongly non-uniform field),^{25, 26, 31, 32} NPs with both broadband absorption and self-constructed multiple hotspots are desired for energy-efficient photocatalysis, but only with limited realizations in nanoporous metals.³³⁻³⁵

The concept of fractals may meet this challenge. Fractal geometry describes a structure with exact or quasi self-similarity.^{36, 37} In nature, there are various fractal-like architectures, such as snowflakes, tree branches, and corals. Stimulated by this concept, plasmonic fractals were investigated because they can introduce tunable multiband resonances and expand the spectral region of their strong optical response,³⁶ overcoming the limitation of the narrow spectral domain in conventional plasmonic antennas.^{38, 39} Despite the successful implementation of fractals in plasmonic applications such as terahertz resonators,^{40, 41} optical antennas,^{42, 43} non-linear optics,^{44, 45} surface-enhanced Raman scattering (SERS),⁴⁶⁻⁵⁰ energy harvesting,⁵¹ and photodetection,^{52, 53} there are still several major obstacles in utilizing them for photocatalysis: (i) sophisticated fabrication methods based on the use of expensive methods, such as focused ion beam lithography, electron beam lithography, and direct laser writing,⁵⁴ is impractical for photocatalysis, which typically requires freestanding NPs instead of plates attached on substrates and scalable production. (ii) the spatial origin of the broad-band response and hotspots, and their relevance with the geometry are not adequately revealed. (iii) the investigation of hot electron generation at the single-particle level during the photochemical reaction process remains challenging.

Taking advantage of the scalable nature of bottom-up synthesis, we design and chemically synthesize freestanding silver fractals with strong light-matter interactions covering a broad range of the spectrum (400 nm -1100 nm). The varied lengths/widths/curvatures of branches provide not

only broadband resonances, but also multiple self-constructed hot spots through coupling between the protrusions in a single branch or between adjacent branches. Compared to hot spots formed by interparticle coupling, the number of hotspots in our fractals is increased by nearly two orders, proved by both numerical simulations and electron energy loss spectroscopy (EELS) measurements. Combined EELS with dark field spectra and pump-probe measurements at the single-particle level, the plasmonic origin, and their decay dynamics were clearly revealed. Three-dimensional (3D) fractal structures offer enhanced capabilities irrespective of both the incident angle and the polarization of light, as confirmed by the polarization-dependent SERS experiments on an individual fractal. Benefiting from the fractal geometry, the broadband response and strong enhancements in both the magnitude and volume are realized.

To directly access the hot-electron generation rates at different wavelengths, two hot carrier drove chemical reactions: the dimerization of para-nitrothiophenol (*p*NTP) and hydrogen evolution were carried out and hot electron generation on individual particle was proved under visible irradiation. We firstly demonstrated a broadband improvement of the reaction rate of the dimerization of *p*NTP, a 60-fold improvement at 785 nm excitation comparing to aggregated spheres. Besides, we found the hydrogen generation rate of fractal/TiO₂ is ~ 6.7 times higher than that of pure TiO₂ sample. The synthesized fractals offer a significantly increased hot-electron generation rate, and anisotropic broadband optical response, providing a promising candidate not only for plasmonic-assisted photocatalysis and energy harvesting but also for sensing, disease diagnosis, and treatment.

RESULTS AND DISCUSSION

Design and Modelling of Dendritic Silver Fractals. We selected a dendritic structure composed of a large branch with several attached twigs as the building block, (Figure 1a), which share the

same shape but with different sizes, providing the self-similarity typical of fractals. To effectively harvest light with different polarizations, we duplicate the dendrite along with different directions, obtaining a fractal particle. The high rotational symmetry guarantees the isotropic optical response of the structure.

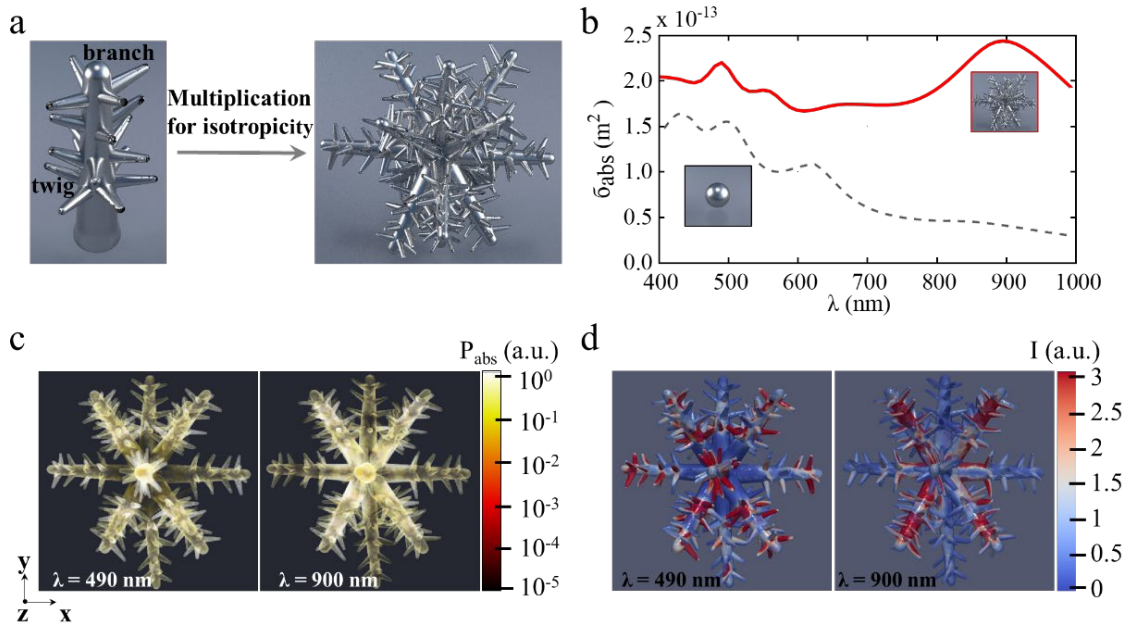


Figure 1. Modelling of bio-inspired dendritic silver fractal particle. (a) Schematics of the fractal NP. (b) Calculated absorption cross-section σ_{abs} of the fractal particle (red solid line) and a sphere with the same volume as a reference (black dashed line). (c) Calculated spatial distribution of absorption power density P_{abs} at both visible and NIR wavelengths. The left panel shows the case of 490 nm and the right panel shows the case of 900 nm. (d) The light intensity I distribution on the particle surface from simulations. The left panel shows the case of 490 nm and the right panel shows the case of 900 nm.

To investigate the optical properties of the fractal particle, we implemented full-wave simulations with results summarized in Figure 1b-d. Figure 1b shows the calculated absorption cross-section σ_{abs} of the particle, covering the visible to the NIR ranges. Broadband absorption is

achieved, and the value of σ_{abs} varies slightly in the wavelength range (400-1000) nm, with an average value of $\sigma_{\text{abs}} = 1.72 \times 10^{-13} \text{ m}^2$ with a standard deviation of $\pm 4.4 \times 10^{-14} \text{ m}^2$. On the other hand, we selected a spherical particle with the same volume as the proposed fractal as a reference. The absorption cross-section of the sphere was calculated from Mie theory³⁰ and it is shown in Figure 1b as a black dashed line, with a low value of σ_{abs} beyond 700 nm. A prominent absorption enhancement of more than 50% is confirmed by comparing the two geometries. Meanwhile, a 5-fold enlargement of the surface area is achieved from sphere to fractal, providing more active regions for the chemical reactions.

In addition to exhibiting a broadband plasmonic resonance, the dendritic fractal can concentrate light into densely localized EM field regions, *i.e.*, hotspots. Figure 1c provides more details of the broadband absorption by illustrating the spatial distribution of absorption power density P_{abs} inside the fractal particle. Two different wavelengths are chosen respectively, matching the absorption. At shorter wavelengths (*i.e.* $\lambda = 490 \text{ nm}$), strong absorption is achieved at the small twigs while the big branches can effectively capture photons at longer wavelengths (*i.e.* $\lambda = 900 \text{ nm}$). As a total effect, the self-similarity induces a broadband optical response, harvesting photons from the visible to the NIR range. Figure 1d highlights the simulated light intensity at the surface of the particle. Multiple hotspots are naturally generated at different locations within the fractal at both wavelengths, taking advantage of its dendritic shape. The self-similarity not only induces the broadband absorption but also concentrates photons of different wavelengths into the same hotspot, benefiting the light-harvesting from a broadband source (Figure S1). A large number of hotspots effectively concentrates photons into multiple active sites, boosting hot electron production for photocatalysis.⁵

Synthesis and Plasmonic Properties of Silver Fractals. Dendritic silver fractals were

synthesized from solution process with a modified strategy.^{49, 50, 55} Briefly, ascorbic acid was added to a silver nitrate aqueous solution under stirring and then the grey particles appear spontaneously as shown in Figure 2a. The morphologies of several dendritic silver fractals are shown in Figure 2b and Figure S2a. As revealed by scanning electron microscopy (SEM) images, the morphology of the particles can be described as repeated rod-like units that assemble into dendritic fractals with randomly arranged protrusions and narrow gaps. Their crystal structure is obtained through transmission electron microscopy (TEM) and reported in Figure S3, revealing a typical face-centered cubic structure. It is necessary to note that based on the nature of chemical synthesis, the precise control over the morphology and dimensions of the final product is limited for fractal-type of structures, which is a restriction for its shape/size uniformity. However, their fractal features are highly similar with good reproducibility between different synthesized batches. The absorbance spectra of ensemble particles in the colloidal phase and scattering spectra of individual particles on a substrate are shown in Figure 2c and S4. While we normalize the single particle extinction spectra for the ease of comparison, the extinction spectra in Fig. 4a are measured based on two liquid ensembles with the same concentration, demonstrating the enhanced extinction of fractals. Fractal structures show broadband plasmonic resonances spanning from 400 to above 1100 nm. The main reason is the varying lengths/widths/curvatures of branches and the randomly arranged gap sizes formed between the protrusions in a single branch or between adjacent branches. This geometrical arrangement leads to multiple plasmonic resonances with different spectral positions and intensities, which overlap with each other to form a broadband continuous extinction spectrum.³⁶ In contrast, individual spheres show one main plasmonic resonance in visible range, which broadens and extends to the NIR range after aggregation of several spheres (Figure S4).

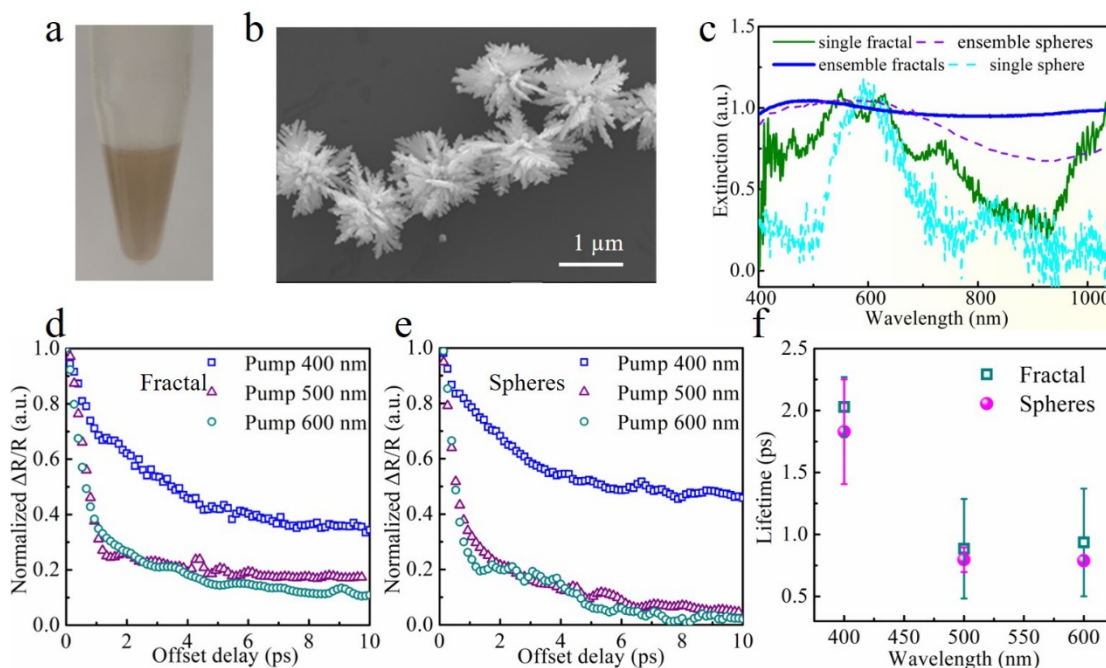


Figure 2. Characterization of dendritic fractals. (a) optical photo and (b) SEM images of silver fractal NPs. (c) Normalized absorbance spectra of ensemble particles in solution and scattering spectra of individual particles on the substrate. Pump-probe traces of silver fractals (d) and spheres (e). (f) The lifetime of silver fractals and spheres pumped at different laser wavelengths. Error bars represent the standard deviation of measurements in multiple clusters.

Non-degenerate pump-probe measurements in the *vis*/NIR range were conducted to investigate the ultrafast hot carrier dynamics in both kinds of plasmonic structures (Figure 2d-f).⁵⁶ Samples were prepared by drop-casting the solution containing either the Ag fractals or the Ag spheres on a common glass slide substrate, and were left for dry before measurements. Experiments were performed in aggregated dendritic silver fractals and spheres as a reference, which also produce several hotspots at the touching point among spheres, as the modulated probe signal was too weak when measuring single nanostructures. When pumping/probing at 400/800 nm, a slow decay (~2 ps) was observed for both samples, a modulation attributed to thermal electron-phonon scattering

of intraband excited electrons.⁵⁷ While, a faster dynamic was observed when pumping/probing the sample at 500/1000 nm and 600/1200 nm wavelengths, with average lifetimes < 1 ps for both samples, which is attributed to the excitation of a large population of hot-electrons mediated by the huge field confinement in the hot-spots (Landau damping). As such non-thermal electron-electron scattering contributes significantly to the signal.⁵⁸⁻⁶⁰ Limited by available setups, we implemented pump-probe measurements constrained to a harmonic as a probe and the corresponding second harmonic as a pump. A complete transient absorption spectroscopy⁶⁰ with probe wavelengths covering the visible may provide a panorama of the dynamics of non-thermal carriers.

Note that similar decay behaviors were observed for both the spheres and fractals, which stems from a large number of small gaps and hot-spots generated in the former upon aggregation. It has been shown that tips and sharp corners are the regions emitting the higher energy carriers.¹² In this sense, the dendritic character of these fractal structures provides two main advantages: sharp tips all over the structure and enormous surface area, both requirements for utilizing the hot-carriers. Further discussion and examples are shown in the photocatalysis section.

High-Resolution Imaging of Multiple Hotspots on an Individual Fractal. To explore with high spatial resolution the distribution of plasmonic hotspots in the silver fractal nanostructures, we performed EELS measurements. Figure 3a shows the EELS results of a single fractal and a single spherical silver NP. Spectrum No. 1 in Figure 3a (magenta line) indicates the electron energy loss probability of a region further away from the silver dendrite. No significant EEL activity is observed; this spectrum is then used as the reference spectrum. Spectrum No. 2 (red line) is the EEL probability of a selected area around the spherical NP and spectra No. 3 to 7 in Figure 3a are representing the EEL probability of different selected regions of the fractal structure as highlighted

in the TEM images of the inset. According to the EELS data, the dendritic structure possesses a broad energy range of surface plasmon responses, from NIR to near-ultraviolet (UV). This is evident from the multitude of peaks in the averaged EEL spectra over the individual branches of the fractal (spectra No. 4 to 7). The abundance of plasmon peaks in the EELS spectra of the fractal structure results in the saturation of averaged EELS response of the whole silver fractal NP over the entire (~ 1 eV to ~ 3.5 eV) energy window; see Figure 3a spectrum No. 3 in violet.

To better explore the effect of the differently sized nanofeatures on the broadband plasmon response of the dendritic fractal, different regions of a single branch are studied in Figure 3c. The distribution of plasmon peaks in spectra No. 3 to 7 suggests that the surface plasmon responses are highly localized in the branch, and very distinct from point to point due to the diverse geometry of the dendrites. In this regard, as shown by spectrum No. 2 in Figure 3c, the broadband surface plasmon activity is even observed in an individual silver fractal branch.

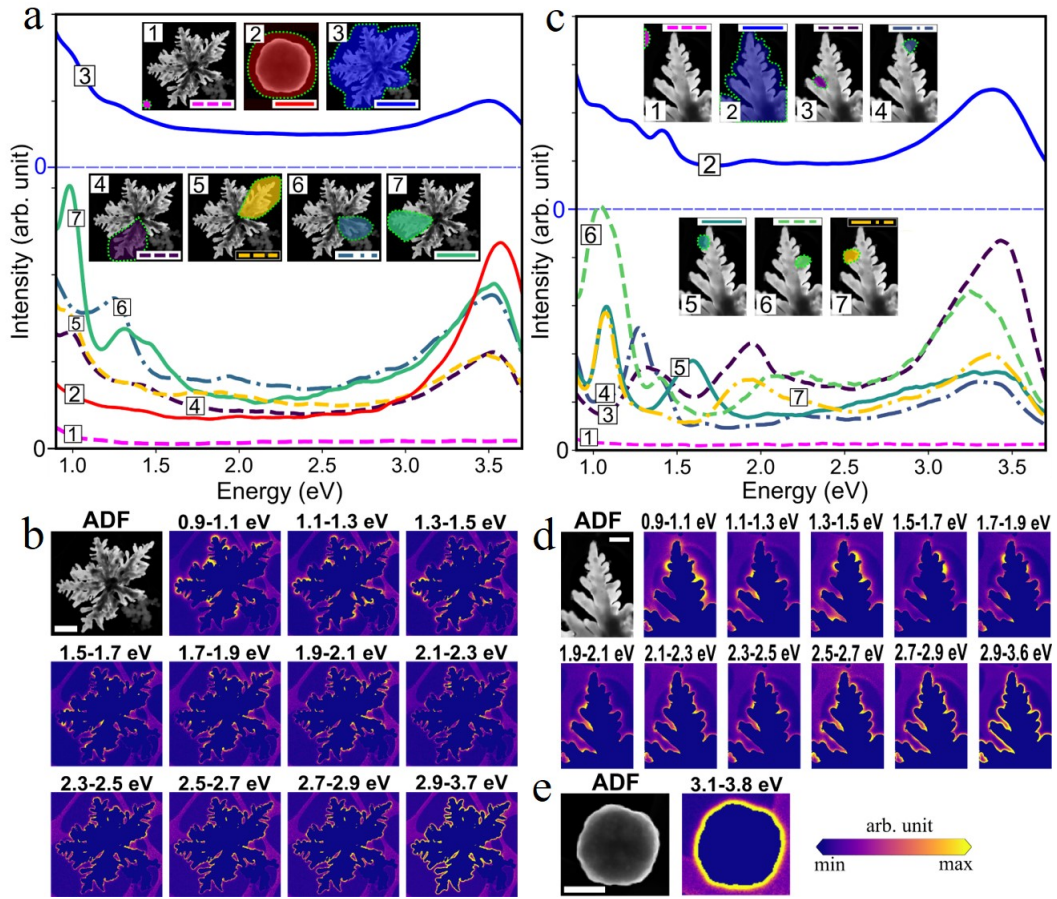


Figure 3. EELS measurements of a single fractal particle and a spherical particle. (a) EEL spectra extracted from selected areas on a silver fractal, shown in the insets, after 10 iterations of the Richardson-Lucy algorithm. **(b)** Annular dark-field image (scale bar = 500 nm) and EELS intensity maps of a single fractal particle averaged over the energy ranges indicated. **(c)** EEL spectra extracted from selected areas on a single branch of a silver fractal nanostructure, shown in the insets, after 10 iterations of the Richardson-Lucy algorithm. **(d)** Annular dark-field image (scale bar = 200 nm) and EELS intensity maps of a single branch of a fractal particle averaged over the energy ranges indicated. **(e)** Annular dark-field image (scale bar = 500 nm) and EELS intensity maps of a single spherical nanoparticle averaged over the energy ranges indicated. For better visualization of the average EELS response of

the whole structures, spectrum No. 3 in (a) and spectrum No. 2 in (c) are shifted in the vertical axis for clarity. A threshold was applied to remove low-intensity pixels from the averaged spectra to reduce the noise, which is emphasized in the Richardson-Lucy deconvolution algorithm.

As is illustrated in Figure 3b and d, the silver fractal EELS maps show EM field enhancement around the silver fractal (which in this case serves to identify the surface plasmon resonances) in the entire depicted energy range (~ 1 eV to ~ 3.5 eV). These enhanced field domains are primarily localized around individual protrusions from the fractal branches (~ 1 to ~ 2.5 eV); at higher energies (above ~ 2.5 eV), these domains are present throughout the fractal structure. The large peak above 3.5 eV is present across the whole surface of the structure and can be attributed to the response of the surface plasmon polariton. In contrast, the spherical NP shows a much lower plasmon response relative to the fractal structure in the same energy window (Figure 3a); this structure only demonstrates a large surface plasmon polariton response above 3.5 eV (Figure 3e).

The results presented corroborate the fact that the hierarchical structure inherent to the dendritic fractal supports a broadband surface plasmon response, with resonances occurring at different length scales across the fractal, ranging from the whole structure at low energy to localized responses on the smallest fractal features at higher energy. The variety of length scales in the fractal structure and the random arrangement of fractal components mean that multiple peaks are present within a given energy range, localized on different areas of the structure in regions of different local geometries.

Photocatalysis of Dimerization of *p*NTP molecules. As mentioned earlier, hot electrons produced by plasmon decay can participate in chemical reactions by being injected into adsorbed species directly for photoreduction reactions, or being transferred to electron acceptors and keep

the holes for photooxidation reactions.^{61, 62} Monitoring plasmonically induced photocatalytic reactions by *in-situ* SERS has been demonstrated as a powerful tool for evaluating the plasmonic reactivity at the single-particle level.^{63, 64} Here, the reaction on a single fractal particle was monitored *in-situ* by a confocal Raman spectrometer as illustrated in Figure 4a and Table S1. Lasers emitting at different wavelengths were used as both excitation and probe sources, and a labelled silicon wafer was used as the substrate to identify the location of measured NPs, as demonstrated in Figure S5. The dimerization of *p*NTP to form DMAB, triggered by hot electrons, was chosen as a model reaction for this proof-of-concept study (Figure 4b).

As recently shown, low energy carriers (with energies on the order of ~ 0.15 eV) can initiate this reaction.⁶⁵ Considering that the maximum (theoretical) energy that a hot-carrier can harvest is the same as that of the incident wavelength,^{9, 66} this low energy barrier reaction serves as a perfect probe to test a broadband absorber catalyst as this one. In this reaction, the hot electron can be directly injected into the adsorbed *p*NTP molecules to drive the -NO₂ group to react with the water absorbed on the silver surface to dimerize into a DMAB molecule.⁶⁷ Silver fractals and spheres can be used as both SERS substrates for signal amplification and as photocatalysts to trigger the reduction reaction simultaneously.

As shown in Figure 4f-i, before illumination ($t = 0$ min), the SERS spectrum is dominated by a peak centered at 1346 cm^{-1} originated from the N-O strength of *p*NTP on a single silver fractal and aggregated spheres. It is important to highlight that no Raman signal can be detected on single silver spheres, due to their low near field enhancement. For this reason, the aggregated spheres with a similar size to a single fractal were used as a comparison. It is noteworthy that benefiting from the complex 3D geometry of fractal, multiple hot spots generated by the self-coupled gaps and sharp tips contribute to an average enhancement factor (EF) of $\sim 10^7$, which varied slightly

with the change of incident light wavelength. (Figure S6) Moreover, SERS enhancement capabilities are independent of the excitation polarization because of the random distribution of hot spots, (Figure S7) which is a great advantage compared to hot spots between, for example, two-spheres (dimers).⁶⁸⁻⁷⁰ Under 633 nm excitation for 1 min, the characteristic nitrogen double bands (N=N) at 1390 and 1440 cm^{-1} and C-N band at 1143 cm^{-1} of DMAB appeared, which confirmed that amount of DMAB is formed through hot electron-induced reaction. With further irradiation, the Raman peak intensity of the N-O band at 1346 cm^{-1} decays and disappears after 4 min, indicating that *p*NTP has transformed into DMAB completely. (Figure 4g and Figure S8) For the control sample - consisting of aggregated spheres - after illumination for 12 min, the DMAB signals were weak, which indicates that the conversion rate of *p*NTP to DMAB on aggregated spheres is slower than that on the fractal (Figure 4i and Figure S9). Moreover, the signal-to-noise ratio on the aggregated spheres is remarkably lower, which is attributed to the low SERS enhancement resulting from their weak plasmonic activity. While for pure *p*NTP powder, no matter the laser power or time used for illumination, the Raman spectra remain unchanged and no DMAB is formed, suggesting the absence of the photocatalyst. (Figure S10)

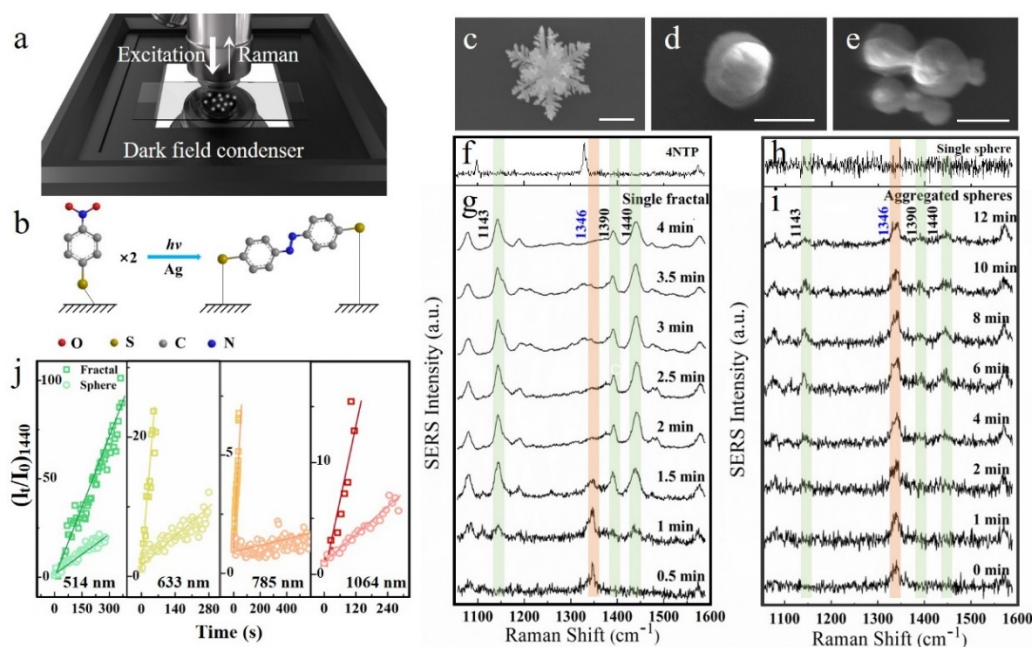


Figure 4. Broadband photocatalysis of *p*NTP dimerization. (a) Experimental setup for Raman and dark field spectra measurements. The objective was used for both laser excitation (Raman) and signal collection (Raman and darkfield). The darkfield condenser was used for white light input during the dark field spectrum measurement. (b) Scheme for the plasmon-catalyzed dimerization of *p*NTP to DMAB under irradiation on the surface of Ag. SEM image and SERS spectra on single silver fractal (c, g), single sphere (d, h), and aggregated spheres (e, i) after irradiation for the different time with 633 nm laser. (f) Raman spectrum of pure *p*NTP molecules. The characteristic Raman bands at 1346 and 1143, 1390, 1440 cm^{-1} are assigned to *p*NTP and DMAB, respectively. All scale bars represent 1 μm . (j) Determination of the rate constant for plasmonic induced reduction reaction of *p*NTP based on the intensity change of the characteristic bands at 1440 cm^{-1} . 514, 633, 785, and 1064 nm laser were used for excitation respectively, and the original SERS spectra are shown in Figure S11.

To investigate the broadband hot-electron generation, the same reaction was tested under different illumination wavelengths. The results are summarized in Figure 4j and Figure S11. Under broadband excitation, the dimerization reactions take place, which confirms the hot electron-induced reactions occur under different wavelengths and with a low activation barrier (it can be triggered by even NIR photons/carriers). When hot electrons are not present (Figure S10, irradiation of pure *p*NTP), whatever laser intensity is applied, it does not induce any chemical reaction, confirming the key role of hot electrons. The reaction speed strongly depends on the laser's power, which was normalized in our experiments for analyzing the reaction kinetics. The reaction rate constant determined by the SERS intensity of the peak at 1440 cm^{-1} is shown in Figure 4j, S11, and table S2, which was described as a function of reaction time vs the ratio between the peak intensity at detected time (I_t) and that at the initial time (I_0). Under the same excitation wavelength, the reaction rate on fractals is higher than that on aggregated spheres. When excitation wavelengths are redshifted, the plasmon-assisted reaction slows down. The ratio of reaction rate between fractals and aggregated spheres was used to determine the photocatalysis efficiency, which is normalized for different particles and different surface areas. The ratio at 514, 633, 785, and 1064 nm was ~10, 20, 60 and 50, respectively. These results demonstrate that broadband plasmonic features allow the flexible use of pumping lasers with wavelengths in a rather broad spectral range (514-1064 nm) and that the strong light-harvesting ability of dendritic fractals lead to greater activity of hot electrons generation and extraction for effective *p*NTP dimerization, compared to single or aggregated spheres, suggesting its potential in promoting plasmon-driven photocatalysis.

Photoelectrochemical (PEC) water splitting and photocatalytic hydrogen generation. For the use of hot electrons, it is essential to harness them before they thermalize or recombine with holes.

When the plasmonic materials are combined with semiconductors, the excited plasmon can generate electron-hole pairs under illumination, and the generated hot electrons transfer over the Schottky barrier to inject into the conductive band of the semiconductor and further participate in chemical reactions. We deposited silver fractals or spheres on TiO₂ spin-coated on fluorine-doped tin oxide (FTO) substrate to form a Schottky junction and assessed their catalytic performance. Three samples, bare TiO₂, sphere/TiO₂, and fractal/TiO₂ were used for comparison. We firstly investigated hot electron generation on individual particles during the PEC water splitting process using a homemade photoelectrochemical cell under optical microscope objective, and the setup and the reaction mechanism were shown in Figure 5a. The TiO₂/Ag electrode is working as the photoanode, and Pt is the counter electrode. Under visible irradiation, the plasmon-induced hot electrons on the photoanode are collected into the circuit under the external bias and transfer to the Pt counter electrode to generate hydrogen, while the holes left in the photoanode participate in oxygen evolution. When the laser beam was focused on the single particle, the photocurrent density-time curves were measured under periodically switched laser illumination. To fairly compare the hot electron effect under tunable light, the laser power and incident angle were the same for all measurements. The laser power is 10 mW/cm², which is insufficient to cause photothermal effect. As shown in Figure 5b and 5c, the photocurrent density of bare TiO₂ is undetectable using irradiation ($\lambda > 420$ nm) with energy below the bandgap of TiO₂ (3.2 eV), confirming the electron transitions between valent and conductive band do not take place (no catalytic reactions happen on bare TiO₂). With silver particle deposition, the photocurrent density of fractal/TiO₂ is ~ 18 nA/cm² under 514 nm irradiation, and ~ 1 nA/cm² under 633 nm irradiation, respectively, which is about one order higher than that of sphere/TiO₂. The origin of the enhanced photocurrent density of fractal can be ascribed from both enhanced light absorption and the

promoted hot electron generation and effective interfacial electron transfer. Noted that, the direct hot electron transfer⁷¹ is not excluded totally, however, it is not dominant in our system.

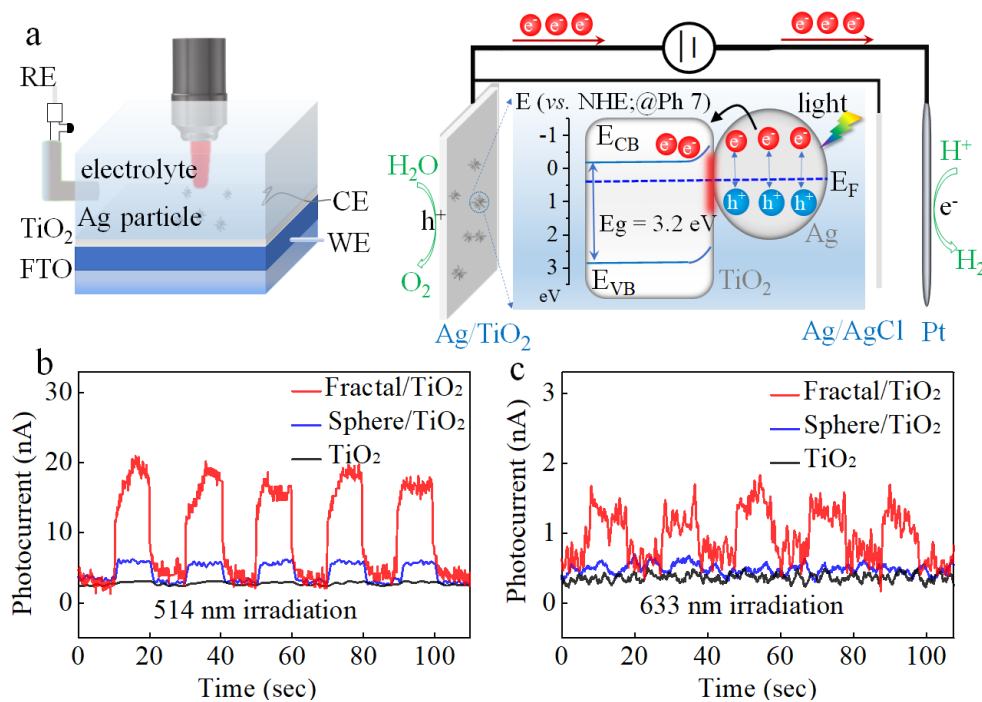


Figure 5. Photocurrent measured on individual silver particles. (a) Schematic illustration of the setup and the proposed mechanism for plasmon induced electron transfer for PEC water splitting. Time evolution of the photocurrent measured on individual silver fractal (b) and sphere (c), respectively.

The performance of silver fractals or spheres deposited on TiO₂/FTO substrate for photocatalytic hydrogen generation was shown in Figure S12. In a sealed reactor with methanol solution (20 vol%) as the sacrificial agent, both UV and visible light (with UV-cutoff filter, $\lambda > 420$ nm) were used for illumination. The hydrogen generation rate of fractal/TiO₂ is ~ 1.2 and 2.1 times higher than that of the sphere/TiO₂ sample, and ~ 2.2 and 6.7 times higher than that of the bare TiO₂ sample. The enhanced performance of fractal/TiO₂ is more significant under visible illumination, which is due to the efficient generation of hot electrons in plasmonic fractals. Noted that, the large surface

area of fractal plays an important role in improving the light absorption and consequently the hot electron generation, which also contributes to the enhanced catalytic activity.

CONCLUSIONS

We prepared free-standing dendritic fractals through a facile chemical process. The plasmonic features of individual fractals were systematically studied through both theoretical simulations and experimental measurements. Silver fractals exhibited multiple LSPRs across the *vis*-NIR range and randomly distributed hot spots, which support independent SERS under different wavelengths with EF as high as 10^7 . Moreover, the hot spots in the Ag fractal structure enhance the generation and extraction of hot electrons, which is confirmed by monitoring the dimerization reaction of *p*NTP molecules and photocatalytic hydrogen generation, shedding light on efficient usage of the total spectrum of solar energy. Considering the broad applications of hot-electron-based devices, the idea of utilizing a fractal geometry may inspire the design in other platforms for a rich manifold of devices including photovoltaics and photodetection, which can benefit from broadband and multiple hotspots with huge field enhancements.

METHODS

Chemicals and Materials. Silver nitrate (AgNO_3 , 99%) and *p*NTP were purchased from Sigma-Aldrich. Titanium (IV) isopropoxide ($\text{C}_{12}\text{H}_{28}\text{O}_4\text{Ti}$, 97%) was purchased from Merck. L-ascorbic acid (L-AA, 99%), nitrate acid, methanol, and ethanol were purchased from Da Mao chemical reagent factory. Deionized water (Millipore) with a resistance of $18.2 \text{ M}\Omega$ was used in all experiments.

FEM Simulations. We performed numerical simulation using COMSOL Multiphysics. Refractive indices of Ag were taken from ref.⁷² The fractals NPs branches are modeled as a truncated cone, with radius (R_0) 65 nm and height (H_0) 480 nm. The top of the cone, with radius (r_0) 32.5 nm, is truncated and replaced by part of a sphere tangent to the cone. A fractal NP is composed of 14 branches. To model the imperfection during the synthesis, the value of R , H and h fluctuates $\pm 7.5\%$ of the averaged value. The cross-section goes to an ellipse instead of a circle. The origination of the branch also fluctuates within $\pm 5^\circ$. On each branch, 19 twigs with similar shape are embedded. The radius (height) of the cone is $R_1 = 34$ nm ($H_1 = 100$ nm) and the height of the truncated cone (h_1) is 17 nm. Similar geometric disorder is embedded in all twigs.

Synthesis of Ag Particles. Before all synthesis, the glassware and stirring bars were soaked in nitrate acid for 30 min, then rinsed with deionized water for seven times until no acid residues left. In a typical synthesis, 0.05 mL of 0.1 M AgNO_3 aqueous solution and 7.5 mL water were mixed in a 25 mL beaker under gentle stirring at 30°C . Then 2.6 mL of 0.2 mM L-AA (ascorbic acid) aqueous solution were added swiftly. The reaction was continued for 10 min. Then, the grey product was collected by centrifugation at 3000 rpm for 2 min and then washed several times with alcohol/water mixture for further characterization. By changing the concentration of reagents, the morphologies of products can be modified.

Preparation Thin Film of TiO_2 . The TiO_2 film was prepared by a sol-gel synthesis and spin coating method.²⁹ The titanium precursor solution was prepared by dissolving 6.1 mL titanium (IV) isopropoxide into 40.6 mL ethanol under vigorous stirring. After 30 min, a mixture of 17 mL ethanol, 0.27 mL water, and 0.196 mL 68 wt% HNO_3 were added drop by drop into the titanium precursor solution for hydrolysis. After 20 h under stirring, the precursor solution was spin-coated on washed FTO substrate at 3500 rpm for 30 s. Then the TiO_2/FTO film was calcined for 2 h at

500°C.

Characterization. The morphology of the samples was characterized by SEM. The crystal structure was determined by a JEOL Model 2100F TEM equipped with the selected area electron diffraction (SAED) detector. The ensemble extinction spectra were measured on the UV-*vis*-NIR spectrometer. The dark field scattering spectra of a single-particle were carried out on a confocal microprobe microscope Raman spectrometer (Renishaw Invia).

Pump-probe. Pump and probe beams were selected as the second harmonic and the fundamental output beams, respectively, of a collinear optical parametric amplifier ORPHEUS-HP (Light Conversion Ltd.; pulse duration of ~180 fs, repetition rate of 200 kHz) coupled to a pulsed Yb:KGW Pharos laser system. Measurements were taken in reflection mode using a 40×, NA 0.6 objective. A 5 μW pump power was used for all excitation wavelengths, and the pump-probe fluence ratio was kept at 5:1. A motorized optical delay line, with an accuracy <1 fs, was used to introduce a controlled time difference between pump and probe beams. Measurements were carried out with lock-in detection by modulating the pump beam with a mechanical chopper at <1-kHz frequency. A spectrograph (PI Acton SP2300 by Princeton Instruments) coupled to a low-noise Si photodiode (picowatt photoreceiver series PWPR-2K by Femto) was used for the detection of the probe beam reflected by the sample. An InGaAs photodiode (DET10C2 by Thorlabs) was used for probe beam detection when pumping/probing at the wavelengths of 600/1200nm.

EELS. Electron energy loss spectroscopy data was acquired on a double-corrected, monochromated FEI Titan scanning transmission electron microscope (STEM) equipped with a Gatan Quantum spectrometer. The microscope was operated at 80 keV with an energy resolution of approximately 60 meV, as defined by the full width at half maximum of the zero-loss peak. To

prepare the sample for STEM studies, the particles were dispersed in ethanol, sonicated, and deposited on a lacy carbon grid. The Richardson-Lucy deconvolution algorithm was used to increase the effective energy resolution of the spectra to approximately 35 meV. The Richardson-Lucy deconvolution algorithm enhances noise in low-intensity pixels, so an intensity threshold was applied prior to deconvolution and spectrum averaging to reduce the contributed noise. Data analysis was done with a custom software, SpectrumImageAnalysisPy.⁷³ To reduce the high-frequency noise in the EELS signal, all spectra are filtered using the Savitzky-Golay filtering algorithm.⁷⁴

Raman and photocatalysis of dimerization of *p*NTP molecules: Silver particles were incubated in 10⁻³ M *p*NTP solution overnight in dark to allow self-assembled monolayers' adsorption and then they were washed by the mixture of water and ethanol 3 times to remove the un-absorbed molecules. The washed particles were resuspended in ethanol and then dispersed on the marked silicon wafer for further investigations. *In-situ* Raman and photocatalysis were carried out with a confocal Raman system (Renishaw Invia). The 100× objective with an N.A. = 0.9 was used for signal collection. Different wavelengths of laser source were used for initiated the reaction and excited SERS. To estimate the EF of SERS, we follow the methods as previously reported.^{50, 70}

Calculation method of SERS EF. The EF of surface-enhanced Raman signal was calculated following the equation (1) as reported previously:^{50, 70}

$$EF = \frac{I_{SERS}}{I_{bulk}} \times \frac{N_{bulk}}{N_{SERS}} \dots\dots\dots(1)$$

where I_{SERS} and I_{bulk} are the characterized peak intensities at 1346 cm⁻¹ of Raman signal collected from an individual nanostructure and a dense molecule powder, while N_{SERS} and N_{bulk} are the numbers of detected molecules of plasmonic structure and in the molecule powder respectively, which are calculated following the equation (2) and (5), respectively.

$$N_{bulk} = \left(\frac{V \times d}{M_w} \right) \times N_A = \left(\frac{\pi \times D^2 \times f \times d}{4M_w} \right) \times N_A \dots \dots \dots (2)$$

Where V is the detected volume, calculated based on the lens's focus diameter D and depth f , which is calculated based on the equation (3) and (4), respectively.

$$D = \frac{1.22\lambda}{NA} \dots \dots \dots (3)$$

$$f \approx \frac{2.53\lambda}{NA^2} \dots \dots \dots (4)$$

where λ is the excitation wavelength and NA is the numerical aperture of the lens. The lens used for collection was 100× with NA = 0.9 for nanostructures, and 50× with NA = 0.5 for dense molecule powder and the calculated D and f values are listed in Table S1. d is the density of p NTP, which is 1.362 g/cm³. M_w is the molecular weight of p NTP, which is 155.17 g/mol, and N_A is Avogadro's number (6.02×10²³ mol⁻¹).

$$N_{SERS} = \frac{A \times \eta}{S} \dots \dots \dots (5)$$

where A is the surface area of active hot spots on plasmonic structures (~1.87×10⁻¹³ m²), η is the coverage of molecules which is estimated as 80%, and S is the size of p NTP molecules which is reported to be 0.2 nm².⁷⁵

Based on the equation, the average EF calculated from at least 10 samples.

Photoelectrochemical water splitting. The photocurrent of single particles was measured in a homemade photoelectrochemical cell with a three electrodes system. A Pt wire was used as a counter electrode (photocathode), the Ag/AgCl in 3M KCl was used as a reference electrode and the TiO₂ spin-coated on FTO substrate with or without deposited Ag particles was used as a working electrode (photoanode). The electrolyte was 0.5 M Na₂SO₄ and the 514 nm and 633 nm laser with a power of 10 mW/cm² were used as excitation under the optical microscope objective.

The laser was focused on individual fractals or aggregated spheres with similar sizes of individual fractals through a water immersion objective (63 x , NA = 0.9). The photocurrent density-time ($J-t$) curves were collected by an electrochemical workstation (Autolab) under light irradiation.

Photocatalytic water reduction for hydrogen generation. 1 mg silver spheres or fractals were drop-casted on 1x1 cm² TiO₂/FTO film for photocatalytic measurements. The sample was placed inside a gas-tight 75 mL reactor with a quartz window. 5 mL methanol solution (20 vol%) was used as the sacrificial agent, both UV light ($\lambda = 260\sim 380$ nm, 9.05 mW/cm²) and visible light (with UV-cutoff filter, $\lambda > 420$ nm, 300 mW/cm²) were used for illumination. Before reaction, the reactor was purged with argon gas for 30 min to remove dissolved oxygen. The reaction temperature was kept at 20°C by recycling water, and the amount of hydrogen generation was periodically analyzed *via* gas chromatography (Shimadzu GC-2010 Plus). The detector and columns used for the hydrogen detection are Barrier Discharge Ionization detector and Restek Shin Carbon.

CONFLICTS OF INTEREST

The authors declare no competing financial interest.

ACKNOWLEDGMENT

These authors, X. Wang and C. Liu, contributed equally to this work. This work was supported by the National Natural Science Foundation of China (NSFC No. 51771132). The authors thank Prof. Hongwei for providing Raman spectrometer. C. Liu. and H. Ren. acknowledges the funding support from Humboldt Research Fellowship from the Alexander von Humboldt Foundation. E. Cortés and S. A. Maier acknowledges the funding support from the Deutsche Forschungsgemeinschaft (DFG, German Research Foundation) Centre of Excellence, e-

conversion, and the Bavaria SolTech programme. S. A. Maier additionally acknowledges the Lee-Lucas Chair in Physics.

ASSOCIATED CONTENT

Supporting Information. Supporting Information is available free of charge *via* the Internet at <http://pubs.acs.org>.

REFERENCES

- [1] Brongersma, M. L.; Halas, N. J.; Nordlander, P. Plasmon-Induced Hot Carrier Science and Technology. *Nat. Nanotechnol.* **2015**, *10* (1), 25-34.
- [2] Clavero, C. Plasmon-Induced Hot-Electron Generation at Nanoparticle/Metal-Oxide Interfaces for Photovoltaic and Photocatalytic Devices. *Nat. Photonics* **2014**, *8* (2), 95-103.
- [3] Linic, S.; Aslam, U.; Boerigter, C.; Morabito, M. Photochemical Transformations on Plasmonic Metal Nanoparticles. *Nat. Mater.* **2015**, *14* (6), 567-576.
- [4] Gao, C.; Jiang, Y.; Sun, C.; Han, J.; He, T.; Huang, Y.; Yao, K.; Han, M.; Wang, X.; Wang, Y.; Gao, Y.; Liu, Y.; Yuan, M.; Liang, H.; Multifunctional Naphthol Sulfonic Salt Incorporated in Lead-Free 2D Tin Halide Perovskite for Red Light-Emitting Diodes. *ACS Photonics* **2020**, *7* (8), 1915-1922.
- [5] Gargiulo, J.; Berte, R.; Li, Y.; Maier, S. A.; Cortés, E. From Optical to Chemical Hot Spots in Plasmonics. *Acc. Chem. Res.* **2019**, *52* (9), 2525-2535.
- [6] Hou, W.; Hung, W. H.; Pavaskar, P.; Goeppert, A.; Aykol, M.; Cronin, S. B. Photocatalytic Conversion of CO₂ to Hydrocarbon Fuels *Via* Plasmon-Enhanced Absorption and Metallic Interband Transitions. *ACS Catal.* **2011**, *1* (8), 929-936.
- [7] Mukherjee, S.; Zhou, L.; Goodman, A. M.; Large, N.; Ayala-Orozco, C.; Zhang, Y.; Nordlander, P.; Halas, N. J. Hot-Electron-Induced Dissociation of H₂ on Gold Nanoparticles

Supported on SiO₂. *J. Am. Chem. Soc.* **2014**, *136* (1), 64-67.

- [8] Shi, X.; Ueno, K.; Oshikiri, T.; Sun, Q.; Sasaki, K.; Misawa, H. Enhanced Water Splitting under Modal Strong Coupling Conditions. *Nat. Nanotechnol.* **2018**, *13* (10), 953-958.
- [9] Pensa, E.; Gargiulo, J.; Lauri, A.; Schlücker, S.; Cortés, E.; Maier, S. A. Spectral Screening of the Energy of Hot Holes over a Particle Plasmon Resonance. *Nano Lett.* **2019**, *19* (3), 1867-1874.
- [10] Christopher, P.; Xin, H.; Linic, S. Visible-Light-Enhanced Catalytic Oxidation Reactions on Plasmonic Silver Nanostructures. *Nat. Chem.* **2011**, *3* (6), 467-472.
- [11] Christopher, P.; Xin, H.; Marimuthu, A.; Linic, S. Singular Characteristics and Unique Chemical Bond Activation Mechanisms of Photocatalytic Reactions on Plasmonic Nanostructures. *Nat. Mater.* **2012**, *11* (12), 1044-1050.
- [12] Cortés, E.; Xie, W.; Cambiasso, J.; Jermyn, A. S.; Sundararaman, R.; Narang, P.; Schlucker, S.; Maier, S. A. Plasmonic Hot Electron Transport Drives Nano-Localized Chemistry. *Nat. Commun.* **2017**, *8*, 14880.
- [13] Zhou, L.; Zhang, C.; McClain, M. J.; Manjavacas, A.; Krauter, C. M.; Tian, S.; Berg, F.; Everitt, H. O.; Carter, E. A.; Nordlander, P.; Halas, N. J. Aluminum Nanocrystals as a Plasmonic Photocatalyst for Hydrogen Dissociation. *Nano Lett.* **2016**, *16* (2), 1478-1484.
- [14] Marimuthu, A.; Zhang, J.; Linic, S. Tuning Selectivity in Propylene Epoxidation by Plasmon Mediated Photo-Switching of Cu Oxidation State. *Science* **2013**, *339* (6127), 1590-1593.
- [15] Zhou, L.; Martirez, J. M. P.; Finzel, J.; Zhang, C.; Swearer, D. F.; Tian, S.; Robatjazi, H.; Lou, M.; Dong, L.; Henderson, L.; Christopher, P.; Carter, E. A.; Nordlander, P.; Halas, N. J. Light-Driven Methane Dry Reforming with Single Atomic Site Antenna-Reactor Plasmonic Photocatalysts. *Nat. Energy* **2020**, *5* (1), 61-70.

- [16] DuChene, J. S.; Tagliabue, G.; Welch, A. J.; Li, X.; Cheng, W.; Atwater, H. A. Optical Excitation of a Nanoparticle Cu/P-NiO Photocathode Improves Reaction Selectivity for CO₂ Reduction in Aqueous Electrolytes. *Nano Lett.* **2020**, 20 (4), 2348-2358.
- [17] Zhou, L.; Swearer, D. F.; Zhang, C.; Robotjazi, H.; Zhao, H.; Henderson, L.; Dong, L.; Christopher, P.; Carter, E. A.; Nordlander, P. Quantifying Hot Carrier and Thermal Contributions in Plasmonic Photocatalysis. *Science* **2018**, 362 (6410), 69-72.
- [18] Tian, Y.; de Arquer, F. P. G.; Dinh, C. T.; Favraud, G.; Bonifazi, M.; Li, J.; Liu, M.; Zhang, X.; Zheng, X.; Kibria, M. G.; Hoogland, S.; Sinton, D.; Sargent, E. H.; Fratalocchi, A. Enhanced Solar-to-Hydrogen Generation with Broadband Epsilon-near-Zero Nanostructured Photocatalysts. *Adv. Mater.* **2017**, 29 (27), 1701165.
- [19] Collado, L.; Reynal, A.; Fresno, F.; Barawi, M.; Escudero, C.; Perez-Dieste, V.; Coronado, J. M.; Serrano, D. P.; Durrant, J. R.; de la Peña O'Shea, V. A. Unravelling the Effect of Charge Dynamics at the Plasmonic Metal/Semiconductor Interface for CO₂ Photoreduction. *Nat. Commun.* **2018**, 9, 4986.
- [20] Feng, K.; Wang, S.; Zhang, D.; Wang, L.; Yu, Y.; Feng, K.; Li, Z.; Zhu, Z.; Li, C.; Cai, M.; Wu, Z.; Kong, N.; Yan, B.; Zhong, J.; Zhang, X.; Ozin, G. A.; He, L. Cobalt Plasmonic Superstructures Enable Almost 100% Broadband Photon Efficient CO₂ Photocatalysis. *Adv. Mater.* **2020**, 32, 2000014.
- [21] Yao, K.; Xia, Y.; Li, J.; Wang, N.; Han, J.; Gao, C.; Han, M.; Shen, G.; Liu, Y.; Seifitokaldani, A.; Sun, X.; Liang, H., Metal-organic framework derived copper catalysts for CO₂ to ethylene conversion. *J. Mater. Chem. A* **2020**, 8 (22), 11117-11123.
- [22] Wang, N.; Miao, R.; Lee, G.; Vomiero, A.; Sinton, D.; Ip, A. H.; Liang, H.; Sargent, E. H., Suppressing the liquid product crossover in electrochemical CO₂ reduction. *SmartMat* **2021**, 2 (1),

12-16.

- [23] Naldoni, A.; Guler, U.; Wang, Z.; Marelli, M.; Malara, F.; Meng, X.; Besteiro, L. V.; Govorov, A. O.; Kildishev, A. V.; Boltasseva, A.; ShalaeV, V. M. Broadband Hot-Electron Collection for Solar Water Splitting with Plasmonic Titanium Nitride. *Adv. Opt. Mater.* **2017**, *5* (15), 1601031.
- [24] Rej, S.; Mascaretti, L.; Santiago, E. Y.; Tomanec, O.; Kment, Š.; Wang, Z.; Zbořil, R.; Fornasiero, P.; Govorov, A. O.; Naldoni, A. Determining Plasmonic Hot Electrons and Photothermal Effects During H₂ Evolution with Tin–Pt Nanohybrids. *ACS Catal.* **2020**, *10* (9), 5261-5271.
- [25] Hartland, G. V.; Besteiro, L. V.; Johns, P.; Govorov, A. O. What's so Hot about Electrons in Metal Nanoparticles? *ACS Energy Lett.* **2017**, *2* (7), 1641-1653
- [26] Kong, X.; Wang, Z.; Govorov, A. O. Plasmonic Nanostars with Hot Spots for Efficient Generation of Hot Electrons under Solar Illumination. *Adv. Opt. Mater.* **2017**, *5* (15), 1600594.
- [27] Keith, E.; D., M., Reference solar spectral irradiance: air mass 1.5. *Center, RERD*, **2009**.
- [28] Santiago, E. Y.; Besteiro, L. V.; Kong, X.; Correa-Duarte, M. A.; Wang, Z.; Govorov, A. O. Efficiency of Hot-Electron Generation in Plasmonic Nanocrystals with Complex Shapes: Surface-Induced Scattering, Hot Spots, and Interband Transitions. *ACS Photonics* **2020**, *7* (10), 2807-2824.
- [29] Zhu, H.; Xie, H.; Yang, Y.; Wang, K.; Zhao, F.; Ye, W.; Ni, W. Mapping Hot Electron Response of Individual Gold Nanocrystals on a TiO₂ Photoanode. *Nano Lett.* **2020**, *20* (4), 2423-2431.
- [30] Bohren; C., F.; Huffman; D., R. Absorption and Scattering of Light by Small Particles. *John Wiley & Sons* **1983**.
- [31] Besteiro, L. V.; Govorov, A. O. Amplified Generation of Hot Electrons and Quantum

Surface Effects in Nanoparticle Dimers with Plasmonic Hot Spots. *J. Phys. Chem. C* **2016**, *120* (34), 19329-19339.

[32] Zhang, H.; Govorov, A. O. Optical Generation of Hot Plasmonic Carriers in Metal Nanocrystals: the Effects of Shape and Field Enhancement. *J. Phys. Chem. C*. **2014**, *118* (14), 7606-7614.

[33] Arnob, M. M. P.; Artur, C.; Misbah, I.; Mubeen, S.; Shih, W. 10X-Enhanced Heterogeneous Nanocatalysis on a Nanoporous Gold Disk Array with High-Density Hot Spots. *ACS Appl. Mater. Interfaces* **2019**, *11* (14), 13499-13506.

[34] Graf, M.; J alas, D.; Weissmüller, J.; Petrov, A. Y.; Eich, M. Surface-to-Volume Ratio Drives Photoelectron Injection From Nanoscale Gold into Electrolyte. *ACS Catal.* **2019**, *9* (4), 3366-3374.

[35] Koya, A. N.; Zhu, X.; Ohannesian, N.; Yanik, A. A.; Alabastri, A.; Proietti Zaccaria, R.; Krahne, R.; Shih, W. C.; Garoli, D. Nanoporous Metals: from Plasmonic Properties to Applications in Enhanced Spectroscopy and Photocatalysis. *ACS Nano* **2021**, *15* (4), 6038-6060.

[36] Wallace, G. Q.; Lagugné-Labarhet, F. Advancements in Fractal Plasmonics: Structures, Optical Properties, and Applications. *Analyst* **2018**, *144* (1), 13-30.

[37] Mandelbrot, B. B., The Fractal Geometry of Nature. *W. H. Freeman and Company: New York* **1977**.

[38] Liang, H.; Ren, H; Guo, Y.; Fang, Y.; Shape-Engineered Silver Nanocones for Refractive Index Plasmonic Nanosensors. *Opt. Lett.* **2019**, *44* (15), 3713-3716.

[39] Liang, H.; Rossouw, D.; Zhao, H.; Cushing, S. K.; Shi, H.; Korinek, A.; Xu, H.; Rosei, F.; Wang, W.; Wu, N.; Botton, G. A.; Ma, D. Asymmetric Silver "Nanocarrot" Structures: Solution Synthesis and Their Asymmetric Plasmonic Resonances. *J. Am. Chem. Soc.* **2013**, *135* (26), 9616-

9619.

- [40] Agrawal, A.; Matsui, T.; Zhu, W.; Nahata, A.; Vardeny, Z. V. Terahertz Spectroscopy of Plasmonic Fractals. *Phys. Rev. Lett.* **2009**, *102* (11), 113901.
- [41] Maraghechi, P.; Elezzabi, A. Y. Enhanced Thz Radiation Emission from Plasmonic Complementary Sierpinski Fractal Emitters *Opt. Express* **2010**, *18* (26), 27336.
- [42] Volpe, G.; Volpe, G.; Quidant, R. Fractal Plasmonics: Subdiffraction Focusing and Broadband Spectral Response by a Sierpinski Nanocarpets. *Opt. Express* **2011**, *19* (4), 3612.
- [43] Bellido, E. P.; Bernasconi, G. D.; Rossouw, D.; Butet, J.; Martin, O. J. F.; Botton, G. A. Self-Similarity of Plasmon Edge Modes on Koch Fractal Antennas. *ACS Nano* **2017**, *11* (11), 11240-11249.
- [44] Navarro-Cia, M.; Maier, S. A. Broad-Band near-Infrared Plasmonic Nanoantennas for Higher Harmonic Generation. *ACS Nano* **2012**, *6* (4), 3537-3544.
- [45] Celebrano, M.; Wu, X.; Baselli, M.; Großmann, S.; Biagioni, P.; Locatelli, A.; De Angelis, C.; Cerullo, G.; Osellame, R.; Hecht, B. Mode Matching in Multiresonant Plasmonic Nanoantennas for Enhanced Second Harmonic Generation. *Nat. Nanotechnol.* **2015**, *10* (5), 412-417.
- [46] Yan, F.; Liu, L.; Walsh, T. R.; Gong, Y.; El-Khoury, P. Z.; Zhang, Y.; Zhu, Z.; De Yoreo, J. J.; Engelhard, M. H.; Zhang, X.; Chen, C. Controlled Synthesis of Highly-Branched Plasmonic Gold Nanoparticles through Peptoid Engineering. *Nat. Commun.* **2018**, *9*, 2327.
- [47] Cheng, Z.; Qiu, Y.; Li, Z.; Yang, D.; Ding, S. Cheng, G.; Hao, Z.; Wang, Q. Fabrication of Silver Dendrite Fractal Structures for Enhanced Second Harmonic Generation and Surface-Enhanced Raman Scattering. *Opt. Mater. Express* **2019**, *9* (2), 860-869.
- [48] Wallace, G. Q.; Foy, H. C.; Rosendahl, S. M.; Lagugné-Labarthe, F. Dendritic Plasmonics

for Mid-Infrared Spectroscopy. *J. Phys. Chem. C* **2017**, *121* (7), 9497-9507.

[49] Liang, H.; Li, Z.; Wang, Z.; Wang, W.; Rosei, F.; Ma, D.; Xu, H. Enormous Surface-Enhanced Raman Scattering from Dimers of Flower-Like Silver Mesoparticles. *Small* **2012**, *8* (22), 3400-3405.

[50] Liang, H.; Li, Z.; Wang, W.; Wu, Y.; Xu, H. Highly Surface-roughened "Flower-like" Silver Nanoparticles for Extremely Sensitive Substrates of Surface-enhanced Raman Scattering. *Adv. Mater.* **2009**, *21* (45), 4614-4618.

[51] Han, M.; Wang, N.; Zhang, B.; Xia, Y.; Li, J.; Han, J.; Yao, K.; Gao, C.; He, C.; Liu, Y.; Wang, Z.; Seifitokaldani, A.; Sun, X.; Liang, H. High-Valent Nickel Promoted by Atomically Embedded Copper for Efficient Water Oxidation. *ACS Catal.* **2020**, *10* (17), 9725-9734.

[52] Fang, J.; Wang, D.; Devault, Fang, J.; Wang, D.; DeVault, C. T.; Chung, T.; Chen, Y.; Boltasseva, A.; Shalae, V. M.; Kildishev, A. V. Enhanced Graphene Photodetector with Fractal Metasurface. *Nano Lett.* **2017**, *17* (1), 57-62.

[53] Liu, C.; Mao, P.; Guo, Q.; Han, M.; Zhang, S. Bio-inspired plasmonic leaf for enhanced light-matter interactions. *Nanophotonics*. **2019**, *8* (7), 1291-1298

[54] Duan, H.; Hu, H.; Kumar, K.; Shen, Z.; Yang, J. Direct and Reliable Patterning of Plasmonic Nanostructures with Sub-10-Nm Gaps. *ACS Nano* **2011**, *5* (9), 7593-7600.

[55] Cheng, L.; Ma, C.; Yang, G.; You, H.; Fang, J. Hierarchical Silver Mesoparticles with Tunable Surface Topographies for Highly Sensitive Surface-Enhanced Raman Spectroscopy. *J. Mater. Chem. A* **2014**, *2* (13), 4534-4542.

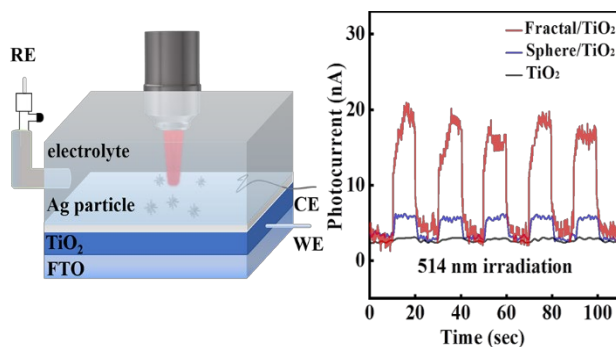
[56] Zhou, D.; Li, X.; Zhou, Q.; Zhu, H. Infrared Driven Hot Electron Generation and Transfer from Non-Noble Metal Plasmonic Nanocrystals. *Nat. Commun.* **2020**, *11*, 2944.

- [57] Hartland, G. V. Optical Studies of Dynamics in Noble Metal Nanostructures. *Chem. Rev.* **2011**, *111*, 3858-3887.
- [58] Heilpern, T.; Manjare, M.; Govorov, A. O.; Wiederrecht, G. P.; Gray, S. K.; Harutyunyan, H. Determination of Hot Carrier Energy Distributions from Inversion of Ultrafast Pump-Probe Reflectivity Measurements. *Nat. Commun.* **2018**, *9*, 1853.
- [59] Khurgin, J. B. How to Deal with the Loss in Plasmonics and Metamaterials. *Nat. Nanotechnol.* **2015**, *10* (1), 2-6.
- [60] Sykes, M. E.; Stewart, J. W.; Akselrod, G. M.; Kong, X.; Wang, Z.; Gosztola, D. J.; Martinson, A. B. F.; Rosenmann, D.; Mikkelsen, M. H.; Govorov, A. O.; Wiederrecht, G. P. Enhanced Generation and Anisotropic Coulomb Scattering of Hot Electrons in an Ultra-Broadband Plasmonic Nanopatch Metasurface. *Nat. Commun.* **2017**, *8*, 986.
- [61] Zhang, Z.; Gernert, U.; Gerhardt, R. F.; Höhn, E. M.; Belder, D.; Kneipp, J. Catalysis by Metal Nanoparticles in a Plug-in Optofluidic Platform: Redox Reactions of P-Nitrobenzenethiol and P-Aminothiophenol. *ACS Catal.* **2018**, *8* (3), 2443-2449.
- [62] Cortés, E. Efficiency and Bond Selectivity in Plasmon-Induced Photochemistry. *Adv. Opt. Mater.* **2017**, *5* (15).
- [63] Zhan, C.; Chen, X.; Huang, Y.; Wu, D.; Tian, Z. Plasmon-Mediated Chemical Reactions on Nanostructures Unveiled by Surface-Enhanced Raman Spectroscopy. *Acc. Chem. Res.* **2019**, *52* (10), 2784-2792.
- [64] Simoncelli, S.; Pensa, E. L.; Brick, T.; Gargiulo, J.; Lauri, A.; Cambiasso, J.; Li, Y.; Maier, S. A.; Cortés, E. Monitoring Plasmonic Hot-Carrier Chemical Reactions at the Single Particle Level. *Faraday Discuss.* **2019**, *214*, 73-87.

- [65] Schurmann, R.; L uxford, T. F. M.; Vinklarek, I. S.; Ko i sek, J.; Zawadzki, M.; Bald, I. Interaction of 4-Nitrothiophenol with Low Energy Electrons: Implications for Plasmon Mediated Reactions. *J. Chem. Phys.* **2020**, *153* (10), 104303.
- [66] Reddy, H.; Wang, K.; Kudyshev, Z.; Zhu, L.; Yan, S.; Vezzoli, A.; Higgins, S. J.; Gavini, V.; Boltasseva, A.; Reddy, P.; Shalaev, V. M.; Meyhofer, E. Determining Plasmonic Hot-Carrier Energy Distributions *Via* Single-Molecule Transport Measurements. *Science* **2020**, *369* (6502), 423.
- [67] Dong, B.; Fang, Y.; Chen, X.; Xu, H.; Sun, M. Substrate-, Wavelength-, and Time-Dependent Plasmon-Assisted Surface Catalysis Reaction of 4-Nitrobenzenethiol Dimerizing to P,P'-Dimercaptoazobenzene on Au, Ag, and Cu Films. *Langmuir* **2011**, *27* (17), 10677-10682.
- [68] Mao, P.; Liu, C.; Favraud, G.; Chen, Q.; Han, M.; Fratalocchi, A.; Zhang, S. Broadband Single Molecule Sers Detection Designed by Warped Optical Spaces. *Nat. Commun.* **2018**, *9*, 5428.
- [69] Liu, Z.; Yang, Z.; Peng, B.; Cao, C.; Zhang, C.; You, H.; Xiong, Q.; Li, Z.; Fang, J. Highly Sensitive, Uniform, and Reproducible Surface-Enhanced Raman Spectroscopy from Hollow Au-Ag Alloy Nanourchins. *Adv. Mater.* **2014**, *26* (15), 2431-2439.
- [70] Kim, J.; Yoo, S.; Kim, J. M.; Choi, S.; Kim, J.; Park, S. J.; Park, D.; Nam, J. M.; Park, S. Synthesis and Single-Particle Surface-Enhanced Raman Scattering Study of Plasmonic Tripod Nanoframes with Y-Shaped Hot-Zones. *Nano Lett.* **2020**, *20* (6), 4362-4369.
- [71] Tan, S.; Argondizzo, A.; Ren, J.; Liu, L.; Zhao, J.; Petek, H. Plasmonic coupling at a metal/semiconductor interface. *Nat. Photonics* **2017**, *11*, 806-812.
- [72] Johnson, P. B.; Christy, R. W. Optical Constants of the Noble Metals. *Phys. Rev. B* **1972**, *6* (12), 4370.

- [73] icbicket Data Analysis: Spectrum Imaging Analysis. *Zenodo* **2017**.
- [74] Savitzky, A. Golay, M. J. Smoothing and Differentiation of Data by Simplified Least Squares Procedures. *Anal. Chem.* **1964**, 36 (8), 1627-1639.
- [75] Xie, W.; Schlucker, S. Hot Electron-induced Reduction of Small Molecules on Photorecycling Metal Surfaces. *Nat. Commun.* **2015**, 6, 7570.

Table of Contents Graphic



We designed and synthesized silver fractal structures with the broadband generation of hot electrons for better matching with the solar radiation spectrum. We directly revealed the plasmonic origin, the spatial distribution, and the decay dynamics of hot electrons on a single-particle level. Hot-electron-triggered dimerization of para-nitrothiophenol and hydrogen production are investigated under various irradiation and the fractals were confirmed with improved efficiency.
